Rayleigh-Taylor Growth Measurements in the Acceleration Phase of Spherical Implosions on OMEGA

V. A. Smalyuk, S. X. Hu, J. D. Hager, J. A. Delettrez, D. D. Meyerhofer,* T. C. Sangster, and D. Shvarts†
Laboratory for Laser Energetics, University of Rochester, 250 East River Road, Rochester, New York 14623, USA
(Received 22 July 2009; published 2 September 2009)

The Rayleigh-Taylor (RT) growth of 3D broadband nonuniformities was measured using x-ray radiography in spherical plastic shells accelerated by laser light at an intensity of $\sim 2 \times 10^{14}$ W/cm^2. The 20- and 24-μm-thick spherical shells were imploded with 54 beams on the OMEGA laser system. The shells contained diagnostic openings for backlighter x rays used to image shell modulations. The measured shell trajectories and modulation RT growth were in fair agreement with 2D hydro simulations during the acceleration phase of the implosions with convergence ratios of up to ~2.2. Since the ignition designs rely on these simulations, improvements in the numerical codes will be implemented to achieve better agreement with experiments.

DOI: 10.1103/PhysRevLett.103.105001 PACS numbers: 52.57.Fg

In inertial confinement fusion (ICF) [1], the spherical target is imploded either directly with laser beams (direct drive) [2] or indirectly by x rays, where the laser drive is converted into x rays inside a high-Z enclosure (hohlraum) [3]. The goal of the implosion is to achieve high compression of the fuel and a high temperature of the hot spot to trigger ignition and maximize the thermonuclear energy gain [1]. The unstable growth of target nonuniformities is one of the most important factors that limit target performance in ICF [1–3]. A direct-drive implosion begins with an acceleration phase when the laser beams ablate the shell's surface and the capsule accelerates and starts to converge. At this stage, outer-shell nonuniformities, both existing imperfections on the shell's surface and imprinted imperfections caused by nonuniformities in the laser drive, grow as a result of the acceleration-phase Rayleigh-Taylor (RT) instability [4–7]. As the shell accelerates, these front-surface perturbations feed through the shell, seeding perturbations on the inner surface. After the laser is turned off, the ablation front becomes stable and the shell starts to decelerate due to inner gas pressure while continuing to converge. At stagnation, the shell stops (peak compression) and then rebounds. During the deceleration phase, the inner surface of the shell is subject to RT instability [8]. Deceleration-phase RT growth results in the mixing [9–14] of cold-shell material with hot-core gas, reducing the target compression and neutron yield. The modulations also grow as a result of Bell-Plesset (BP) convergent effects [15] throughout the compression.

Hydrodynamic growth of target perturbations has been extensively studied in planar geometry using both x-ray [16–18] and direct [4–7,19,20] drives. RT growth rates in the linear regime of instability have been measured using single-mode perturbations [4–7,16,17]. Multimode [18] and 3D broadband [19,20] perturbations were used to measure nonlinear saturation [21,22] and mode-coupling effects. Experiments in cylindrical [23,24] and spherical geometry [25,26] measured the growth of preimposed modulations during the acceleration phase. This Letter presents the first measurements of the RT growth of 3D, broadband modulations during the acceleration phase of a direct-drive spherical implosion. The experimental data were used to validate 2D hydrodynamic simulations and allow a better understanding of the RT growth dynamics during the acceleration phase. This experimental study is critical to the success of ICF because ignition designs rely on these simulations.

In the experiments described here, initially smooth, 860-μm-diam, 20- and 24-μm-thick CH shells were driven with 3-ns square pulses at a laser intensity of $\sim 2 \times 10^{14}$ W/cm^2 on the OMEGA laser system [27]. The shells contained 400- or 600-μm-diam openings that allowed diagnostic x rays from the backlighter to radiograph the shell. Figure 1 presents a schematic of the target showing the spherical shell with the opening and a gold cone that serves as a shield from the laser light entering the inner part of the spherical target. The modulation growth was measured with through-foil x-ray radiography [19] using x rays from three different backlighters: ~1.8-keV samarium,

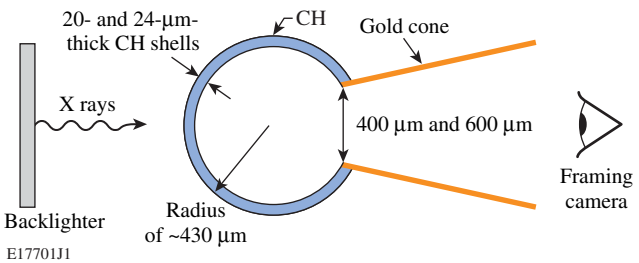

FIG. 1 (color online). Experimental configuration. Spherical 20- and 24-μm-thick CH shells contain 400- and 600-μm-diam openings that allow diagnostic x rays from the backlighter to radiograph the shell. The gold cone serves as a shield from the laser light entering the inner part of the spherical target.

~2.0-keV dysprosium, and ~2.5-keV tantalum. The harder x rays were used at later times when the shell converged to larger areal densities. The backlighter x rays were imaged by an 8-μm pinhole array onto a framing camera that made it possible for multiple images with a temporal resolution of ~80 ps and a spatial resolution of ~10 μm to be captured at different times [19]. The initial target modulations, used for RT-growth measurements, were imprinted by laser-intensity nonuniformities using one beam that arrived ~100 ps before the other drive beams that were used for target acceleration [19,20]. The process of laser imprinting takes about 100 ps [19,20]. During this time, a plasma develops (from laser ablation) between laser absorption (near the critical surface) and ablation surfaces that decouples laser beams from the target, thereby stopping the imprinting process [19]. The spherical targets were driven with 54 overlapping OMEGA beams with smoothing techniques that included distributed phase plates (DPPs) [28], and polarization smoothing (PS) [29]. The backlighter x rays were produced using an additional six OMEGA beams. The part of the shell opposite the shield was driven as in a fully symmetric 1D implosion. This was verified by comparing measured shell trajectories with 1D predictions during the acceleration phase, as shown below.

An optical-depth (OD) image (obtained by taking a natural logarithm of intensity-converted framing-camera images) is shown in Fig. 2(a). The images were used to determine the outer diameter of the imploding shell and were compared with predictions of the 1D hydrocode LILAC [30]. Central 200-μm^2 parts of the images [Fig. 2(b)] were used to measure modulation growth and compare it with predictions of the 2D hydrocode DRACO [31]. A Weiner filter (based on measured system resolution and noise) was applied to these images to remove noise and deconvolve the system's modulation transfer function to recover target OD modulations [19]. The measured target OD variations were proportional to the variations in target areal density $\delta[\rho R]$, $\delta[\mathrm{OD}](t) = \mu_{\mathrm{CH}}(E)\delta[\rho R(t)]$, where $\mu_{\mathrm{CH}}(E)$ is the CH target's mass absorption rate at x-ray energy E used for backlighting and t is the measurement time. The measured target mass absorption rates in undriven foils were 380 ± 30 cm^2/g, 320 ± 30 cm^2/g, and 240 ± 20 cm^2/g for samarium, dysprosium, and tantalum backlighters, respectively [19]. The areal-density modulations $\delta[\rho R(t)]$ were obtained by dividing measured OD modulations by target mass absorption rates. Harder x rays were used to measure modulations at late times because softer backlighter x rays could be completely absorbed in imploding targets, when convergence causes shell areal densities to increase.

Figure 3 compares the measured and simulated shell outer diameters in an experiment with a 20-μm-thick CH shell, showing that the predicted drive by the 1D code is in agreement with that measured. In simulations, the shells were backlit similar to experiments. The position of the outer diameter of the shell was chosen at the half maximum of intensity attenuation profile in the measured and simulated backlit images. Analysis shows that the shell opening has a small effect on the shell convergence at the time of measurement. It justifies using 2D simulations of a symmetric implosion with no opening or shield to compare with measured RT growth. Figure 4 shows an example of 2D simulation of a 24-μm-thick CH shell showing shell-mass-density position and modulations at 2.0 ns. The 2D simulation included DPP-induced modulations in laser drive, shown in Fig. 1 of Ref. [19]. The timing of one drive beam was advanced 100 ps relative to other drive beams, as in the experiment. The DRACO predictions of the drive [32] and RT growth of 2D preimposed modulations [33] were previously validated in planar-target experiments at a laser intensity of $\sim 2 \times 10^{14}$ W/cm^2, the same intensity used in current experiments.

Figure 5 compares the measured and simulated rms of areal-density modulations in experiments with

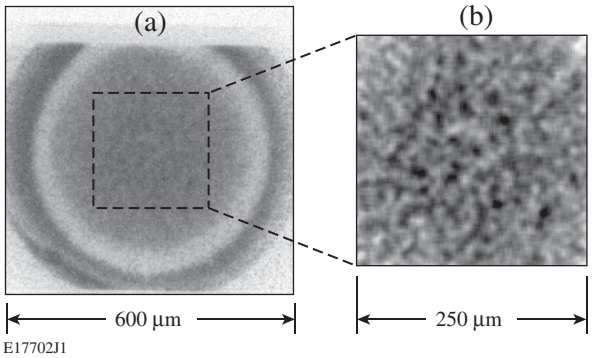

FIG. 2. (a) Example of a face-on radiograph image of the imploding shell used to measure the outer diameter of a target with a 20-μm-thick CH shell. (b) Central 200-μm-sq parts of the image were used to analyze the growth of 3D broadband modulations.

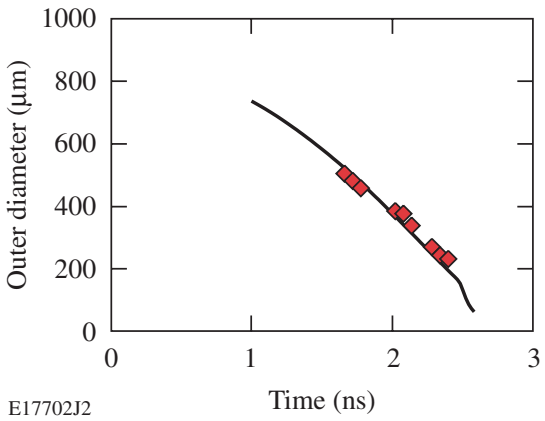

FIG. 3 (color online). Predicted by 1D code (solid curve) and measured (diamonds) outer-shell diameter in the experiment with 20-μm-thick CH shell, showing that the predicted drive is in agreement with that measured.

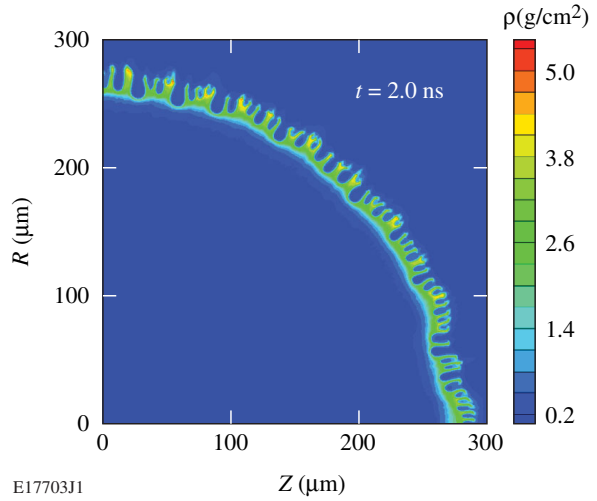

FIG. 4 (color online). An example of a simulation, by the 2D hydrocode DRACO, of a shell-mass-density contour in an experiment with a 24-μm-thick CH shell at 2.0 ns.

24-μm-thick CH shells. The effects of the experimental spatial and temporal resolutions were included in the simulations. The rms modulation grows ~40× from the start of the acceleration phase at 1 ns to the end of the measurements at 2.5 ns. The rms areal-density amplitudes of modulation reach ~1 mg/cm^2 at 2.5 ns and become comparable to the shell's areal density at that time, significantly compromising the shell's integrity. The outer-shell diameter at that time was ~400 μm, and the distance traveled by the shell was ~230 μm with a convergence ratio of ~2.2. Growth measurements were limited to ~2.5 ns because at later times the emission from the imploding target core dominated the backlighter emission, thereby compromising the measurements. The measured and simulated modulation growths are in reasonable agreement. There are small discrepancies in the early part of the drive (where the predicted modulations are smaller than the measurements) and at the end of the drive (where the predicted modulations are slightly larger than the measurements). The modulation spectra in the simulations were limited to ℓ modes up to $\ell = 280$. The reliable simulations with higher ℓ modes are numerically challenging at this time. Three-dimensional effects of the modulation growth may not be properly modeled in the 2D simulations and can contribute to the small discrepancies between the simulation and experiment. Since the ignition designs rely on these simulations, improvements in the numerical codes will be implemented to achieve better agreement with experiments.

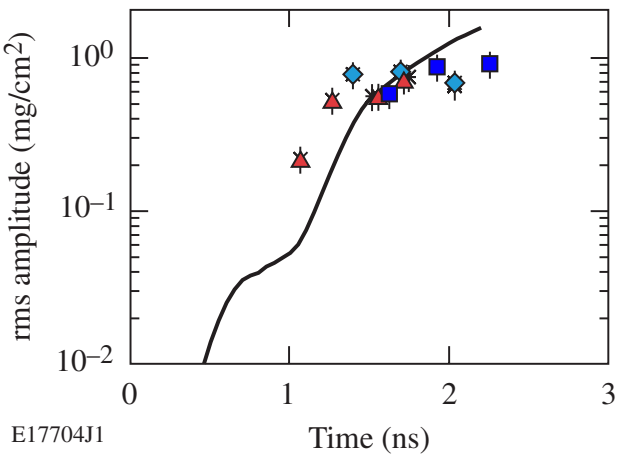

FIG. 5 (color online). Evolution of the simulated (solid curve) measured (in four different shots) areal-density rms amplitude as a function of time in experiments with 24-μm-thick CH shells. Different symbols represent different shots.

Previous experiments with planar targets showed that the average size of modulations shifts to longer wavelengths as the modulations grow in a nonlinear regime [19,20]. Smaller bubbles are overcome by larger bubbles through bubble competition and bubble merger processes [20,34]. The modulation images taken at different times resembled themselves only up to the time when new generations of bubbles were created through bubble merger [20]. In convergent geometry it is expected that the bubble merger processes become faster, compared to planar geometry, because the convergence moves bubbles closer to each other. In this case the modulation images may lose their resemblance faster in spherical geometry than in planar geometry. Figure 6 compares modulation images in (a) spherical and (b) planar geometry at the same level of perturbation areal-density rms of ~0.6 mg/cm^2. Spherical

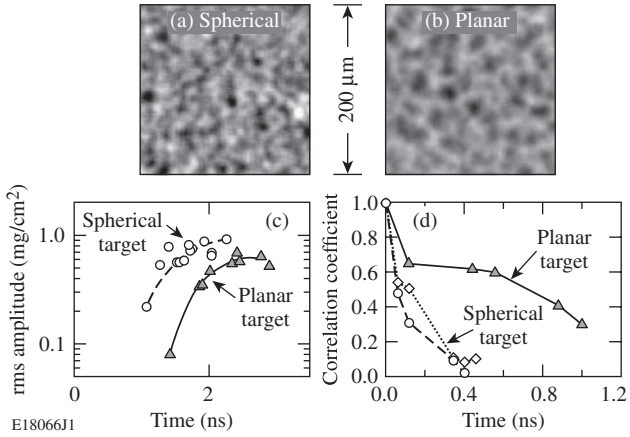

FIG. 6. Measured modulation images in (a) spherical and (b) geometries at the areal-density rms level of ~0.6 mg/cm^2. (c) Measured areal-density rms amplitude as a function of time in experiments with 24-μm-thick CH targets in planar (triangles) and spherical (circles) geometries. The solid and dashed curves show trends in the data. The spherical data are the same as in Fig. 5. (d) Correlation coefficient of the target modulation images as a function of relative time in shots conducted in planar (triangles) and spherical (circles) geometries. Diamonds represent the correlation coefficient when the effect of demagnification caused by spherical convergence was taken into account.

data were taken from Fig. 5 and planar data from Ref. [35], in which planar 24-μm-thick CH targets were accelerated at the same intensity with the same 3-ns square pulse shape, as in spherical experiments. The spatial size of modulations in spherical targets is slightly smaller than in planar targets because of convergent effects. Figure 6(c) compares the areal-density modulation growth in spherical and planar targets showing that modulations have similar growth factors in both cases. The planar-target data are shifted in time by $\sim$0.5 ns because the initial imprinted modulations were smaller in planar experiments (all drive beams were cotimed in planar experiments, while in spherical experiments one beam was advanced in time to increase the imprinting). The spatial correlation of target modulations for sequential images is shown in Fig. 6(d). It shows a comparison of the correlation coefficients as a function of relative timing between images in planar (solid curve) and spherical (dash and dotted curves) experiments. The initial images used in calculating the correlation coefficients were at the areal-density rms level of $\sim$0.4 mg/cm^2 for both planar and spherical geometries. While the correlation among modulation structures in planar-target images persists at least $\sim$1 ns, although it is reduced as the modulations evolve, the correlation between modulations in spherical-target images disappears after $\sim$0.3 ns. Part of the correlation reduction in spherical images is due to convergent effects; convergence makes features smaller as though they are demagnified. The correlation coefficient corrected for demagnification (shown by diamonds) improves the correlation marginally. Possible explanations for the observed difference between spherical and planar geometries are the following: (1) the spatial size of bubbles in planar geometry is larger (as shown in Fig. 6); it takes longer for them to change their shapes. Smaller features can evolve and coalesce faster. (2) Convergence can make small features looked merged due to finite spatial resolution ($\sim$10 μm in these experiments). While these experiments do not provide a definite answer as to whether the merging rates are different in planar and spherical geometries, future experiments will address this question by measuring the merger rates of larger, better-resolved modulations in spherical geometry.

In conclusion, the unstable RT growth of 3D broadband modulations was measured in the acceleration phase of spherical implosions for the first time. The measured shell trajectories were in agreement with 1D predictions, and measured modulation RT growth was in agreement with 2D hydrosimulations during the acceleration phase of implosions with convergence ratios of up to $\sim$2.2. These experimental results are critical to the success of ICF because ignition designs rely on these simulations. The correlation between nonuniformity structures in images of spherically driven targets disappears more rapidly than in planar targets. This suggests that the spherical convergence accelerates bubble merger compared to planar geometry.

This work was supported by the U.S. Department of Energy Office of Inertial Confinement Fusion under Cooperative Agreement No. DE-FC52-08NA28302, the University of Rochester, and the New York State Energy Research and Development Authority.

*Also at Departments of Mechanical Engineering and Physics and Astronomy, University of Rochester, Rochester, NY, USA.

†Also at Nuclear Research Center Negev, Negev, Israel.

[1] S. Atzeni and J. Meyer-ter-Vehn, *The Physics of Inertial Fusion: BeamPlasma Interaction, Hydrodynamics, Hot Dense Matter*, International Series of Monographs on Physics (Clarendon Press, Oxford, 2004).
[2] S. E. Bodner *et al.*, Phys. Plasmas **5**, 1901 (1998).
[3] J. D. Lindl, Phys. Plasmas **2**, 3933 (1995).
[4] K. Shigemori *et al.*, Phys. Rev. Lett. **78**, 250 (1997).
[5] S. G. Glendinning *et al.*, Phys. Rev. Lett. **78**, 3318 (1997).
[6] C. J. Pawley *et al.*, Phys. Plasmas **4**, 1969 (1997).
[7] H. Azechi *et al.*, Phys. Rev. Lett. **98**, 045002 (2007).
[8] V. A. Smalyuk *et al.*, Phys. Rev. Lett. **87**, 155002 (2001).
[9] T. R. Dittrich *et al.*, Phys. Rev. Lett. **73**, 2324 (1994).
[10] M. D. Cable *et al.*, Phys. Rev. Lett. **73**, 2316 (1994).
[11] M. B. Schneider, G. Dimonte, and B. Remington, Phys. Rev. Lett. **80**, 3507 (1998).
[12] P. B. Radha, Phys. Plasmas **9**, 2208 (2002).
[13] S. P. Regan *et al.*, Phys. Rev. Lett. **89**, 085003 (2002).
[14] C. W. Barnes *et al.*, Phys. Plasmas **9**, 4431 (2002).
[15] M. S. Plesset and T. P. Mitchell, Q. Appl. Math. **13**, 419 (1956).
[16] B. A. Remington *et al.*, Phys. Fluids B **5**, 2589 (1993).
[17] K. S. Budil *et al.*, Phys. Rev. Lett. **76**, 4536 (1996).
[18] M. M. Marinak *et al.*, Phys. Rev. Lett. **80**, 4426 (1998).
[19] V. A. Smalyuk *et al.*, Phys. Rev. Lett. **95**, 215001 (2005).
[20] O. Sadot *et al.*, Phys. Rev. Lett. **95**, 265001 (2005).
[21] S. W. Haan, Phys. Rev. A **39**, 5812 (1989).
[22] S. W. Haan, Phys. Fluids B **3**, 2349 (1991).
[23] W. W. Hsing *et al.*, Phys. Plasmas **4**, 1832 (1997).
[24] D. L. Tubbs *et al.*, Phys. Plasmas **6**, 2095 (1999).
[25] C. Cherfils *et al.*, Phys. Rev. Lett. **83**, 5507 (1999).
[26] S. G. Glendinning *et al.*, Phys. Plasmas **7**, 2033 (2000).
[27] T. R. Boehly *et al.*, Opt. Commun. **133**, 495 (1997).
[28] Y. Lin, T. J. Kessler, and G. N. Lawrence, Opt. Lett. **20**, 764 (1995).
[29] T. R. Boehly *et al.*, J. Appl. Phys. **85**, 3444 (1999).
[30] J. Delettrez *et al.*, Phys. Rev. A **36**, 3926 (1987).
[31] P. B. Radha *et al.*, Phys. Plasmas **12**, 056307 (2005).
[32] S. X. Hu *et al.*, Phys. Rev. Lett. **101**, 055002 (2008).
[33] V. A. Smalyuk *et al.*, Phys. Rev. Lett. **101**, 025002 (2008).
[34] D. Ofer *et al.*, Phys. Plasmas **3**, 3073 (1996).
[35] V. A. Smalyuk *et al.*, Phys. Plasmas **14**, 022702 (2007).